Polarization-dependent Purcell enhancement on two-dimensional h-BN/WS_2 light emitter with the dielectric plasmonic nanocavity

Bowen Du[1,2,4^], Yu Li[3^], Meiling Jiang[3], Hongbo Zhang[2], Lishu Wu[2], Wen Wen[2], Zheng Liu[4, 5, 6*], Zheyu Fang[3*], Ting Yu[1,2*]

Keywords: spontaneous emission, h-BN/WS_2 heterostructure, dielectric plasmonic nanocavity, energy transfer, exciton-plasmon coupling.

[1]School of Physics Science and Technology, Wuhan University, Wuhan 430072, China

[2]Division of Physics and Applied Physics, School of Physics and Mathematical Sciences, Nanyang Technological University, Singapore 637371, Singapore.

[3]School of Physics, State Key Lab for Mesoscopic Physics, Peking University, Beijing 100871, China.

[4]School of Materials Science and Engineering, Nanyang Technological University, Singapore 639798, Singapore.

[5]School of Electrical and Electronic Engineering, Nanyang Technological University, Singapore, Singapore

[6]CINTRA CNRS/NTU/THALES, UMI 3288, Research Techno Plaza, Singapore, Singapore

Abstract

Integrating two-dimensional (2D) transition metal dichalcogenides (TMDCs) into dielectric plasmonic nanostructures enables the miniaturization of on-chip

nanophotonic devices. Here we report on a high quality light emitter based on the newly designed 2D h-BN/WS_2 heterostructure integrated with array of TiO_2 nanostripes. Different to the traditional strongly coupled system like TMDCs/metallic plasmonic nanostructure, we firstly employ dielectric nanocaivities and achieve the Purcell enhancement on nanoscale at room temperature. Furthermore, we demonstrate the light emission strength could be effectively controlled by tuning the polarization configuration. Such polarization dependence meanwhile could be proof of resonant energy transfer theory of dipole-dipole coupling between TMDCs and dielectric nanostructure. This work gains experimental and simulated insights into modified spontaneous emission with dielectric nanoplasmonic platforms, presenting a promising route towards practical applications of 2D semiconducting photonic emitters on silica-based chip.

Introduction. The study of 2D TMDCs has experienced a soaring development over the last ten years in both fundamental physics and device applications, owing to their ultrathin thicknesses and excellent properties [1-5]. In particular, TMDCs exhibit the transition from indirect semiconductors in bulk to direct band gap semiconductors in monolayer [6-8]. Due to the remarkably reduced Coulomb screening, monolayer TMDCs possess strong excitonic effects, offering them to be promising candidates for serving as emitter materials in optical applications, such as lasers and spontaneous emitters[9-11]. Although TMDCs exhibit light-matter interactions in the visible- and near-infrared range, the absorption efficiency is still small compared with other light-emitting

materials[8, 12]. Hence making an interaction enhancement becomes a major challenge for TMDCs photonic emitters. Because of the intrinsic mechanical flexibleness of 2D TMDCs, it is possible to integrate TMDCs with photonic cavities, including Fabry-Perot cavity[13], whispering gallery[14], distributed Bragg reflector (DBR)[15] and optical waveguides[16]. In these photonic crystal (PC) cavities, light is trapped by reflections from periodic dielectric structures, which might lead to high quality factors. Nevertheless, the mode volume of those photonic microcavities is determined by the optical diffraction limit and the size of cavity is much larger compared with the atomic thickness of monolayer TMDCs. With the increasing demand for miniaturization and integration in future photonic devices, it is necessary to develop a high-performance light emitter in nanoscale.

Plasmonic nanostructure (PN), which can motivate the collective excitation of conduction electrons to generate a giant electromagnetic field enhancement near the surface of structure, is considered as an excellent-performing nanocavity[17-19]. In contrast to photonic microcavities, optical fields in PNs can be confined into deep subwavelength volumes beyond the optical diffraction limit[20], which could give rise to intensively localized surface plasmon resonances (LSPRs) near the surface of structures due to confined electrons oscillation with the same frequency as the incident light[21, 22]. Consequently, such PNs have been proposed as light-trapping components that can be integrated in emitters to increase the efficiency of SE at the cavity mode[23, 24]. However, this tight confinement can result in serious optical losses and lead to heating, particularly in noble metals. Optimizing this trade-off will be a critical issue for the

development of PNs in photonic applications.

In this work, we report a 2D heterostructure spontaneous emitter integrated with dielectric plasmonic nanocavities. We fabricated TiO_2 nanostripes arrays on a thin Al_2O_3 film as cavities, and chose the monolayer WS_2 as an emitter due to its high emission quantum yield in TMDCs[25, 26]. The few layers h-BN with similar thicknesses to Al_2O_3 film, which is relatively optical transparent[27], was transferred onto the WS_2 to build a symmetric refractive-index environment between the substrate and the upper cladding. In our hybrid system, the modified spontaneous emission (SE) was observed under the excitation of linearly polarized light. Based on the coupling interaction between excitons of monolayer WS_2 and plasmons of the dielectric nanocavity, the emission intensity can be actively controlled by the orientation of linearly polarized light. In contrast to the strong-coupling regime of designed TMDCs/metal nanostructures, where the emission peak might split into two (known as Rabi splitting) [28], the low-index dielectric nanostructure offers a sharp plasmonic resonance with small cavity linewidth and a remarkable Purcell enhancement is achieved at room temperature[29]. In our devices, we develop a new platform for integrated nanoscale photonic emitters based on silica-based chip.

Results and Discussion. *Design of device.* The schematic of the plasmonic hybrid emitter is illustrated in Figure 1a. Here, the low-index dielectric nanocavities were fabricated as the periodic array of TiO_2 nanostripes on the Al_2O_3/Au (10 nm/100 nm) substrate. The thin Al_2O_3 film was pre-deposited to separate Au film and TiO_2 nanostripes as dielectric spacer, so that surface plasmon polaritons (SPPs) can

propagate along the surface of Au film, and interplay with LSPRs near TiO_2 nanostripes to further enhance the localized electric field. Au film was served as a mirror to improve the reflectivity at the same time[30]. For the emitter material part, few layers h-BN and monolayer WS_2 were mechanically exfoliated and transferred by a dry method. In order to prevent defect states from wrinkles and bubbles during the transfer process, we used a polydimethylsiloxane (PDMS) film to pick up the h-BN and WS_2 one by one, and then suspended the h-BN/WS_2 heterostructure onto the nanocavities. Hence the h-BN layer is served as the top layer to protect emitter materials and keep the dielectric environmental symmetry. The scanning electron microscopy (SEM) image of the nanocavity is shown in Figure 1b with an enlarged view inside. The width of each nanostripe is 128 nm with a period of 570 nm, which was fabricated by e-beam lithography (EBL) and followed by a lift-off process, and the total area of the array is 40 μm × 40 μm. Figure 1c shows the atomic force microscopy (AFM) image, where the total thickness of the device is measured below 45 nm including the h-BN/WS_2 layers. The shape and size of nanocavities were carefully designed by the finite-different time-domain (FDTD) modeling, with the enhanced near-field electric field at the lattice plasmon resonance. Hence the simulated cross-sectional absorption of the structure can match the photoluminescence (PL) emission of monolayer WS_2 as shown in Figure 1d. The absorption curve covers the main region of the SE of monolayer WS_2 with a dip well overlapping with the PL peak of monolayer WS_2. As described previously, the array of TiO_2 nanostripes could form a sharp lattice plasmon mode with over 50% absorption rate at 617.8 nm, indicating a higher quality factor Q compared

with other metal plasmonic nanocavities. This precise match means a coupling process could occur at the dip with an enhanced absorption rate. The normal reflection spectra of the nanocavity were measured under excitations of different linearly polarized lasers, which agree well with the simulated data (Supplementary Fig.S1).

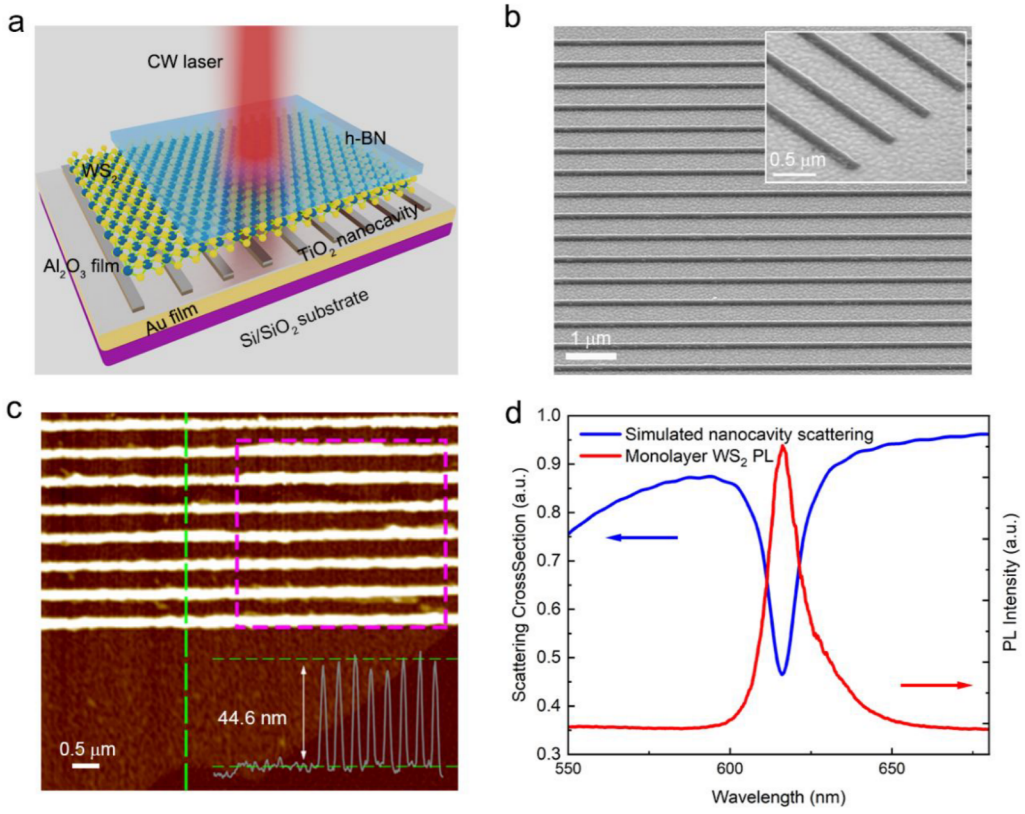

Figure 1. Structure of the h-BN/WS_2 heterostructure spontaneous emitter. (a) Schematic of the h-BN/WS_2 heterostructure spontaneous emitter, excited by the normal incidence laser. (b) SEM images of the TiO_2 nanostripes with an enlarged view inside. (c) AFM image of the device. The height profile of the stripes is obtained through the line scanning along the vertical green dash line. The pink dash block denotes the scanning area for PL mapping. (d) PL spectrum (red line) of monolayer WS_2 and the well-matched nanocavity absorption (blue line) spectrum (simulated). The laser excitation wavelength is 532 nm.

Characteristics of the plasmonic hybrid emitter device. Figure 2a shows the PL intensity mapping of the plasmonic hybrid emitter device, where a continuous-wave 532 nm laser was used for photoexcitation at room-temperature (the scanning area is shown in Figure 1c). The pattern of bright and dark fringes was observed, and the intensity of these fringes demonstrates a clear geometry-dependent distribution along the nanostripes (Supplementary Fig.S2). Monolayer WS_2 emitters exhibit a large SE area for the parts sitting on the nanostripes where strong near-field electric field locates. We labelled the region of the bright fringes as cavity mode (the red dash area in Figure 2a). In contrast, the dark fringes locate at the gap between two nanostripes, where the near-field electric field is very weak, presented as the region of the uncoupled mode (the purple dash area in Figure 2a). Besides, benefited from the increased local density of optical states (LDOS) from the optical confinement at the sub-wavelength scale, this cavity mode leads to significant enhancements in both Raman modes and neutral excitonic emission as clearly seen in the Raman spectra (Figure 2b) and PL spectra (Figure 2c).

It has been widely discussed in previous reports[31] that the optical confinement in hybrid plasmonic nanocavities can substantially influence the spontaneous emission rate due to the Purcell effect. We calculated the Purcell factor F_p, known as the ratio between the modified and free-space emission rates, by the following equation,

$$F_p = \frac{3Q\lambda^3}{4\pi^2 V_0} \quad (1)$$

where, λ is the optical wavelength, Q is the quality factor, V_0 is the cavity mode volume. This formula shows that the modified spontaneous emission benefits from two main factors, cavity mode volume V_0 and quality factor Q. Because light is confined by coupling to electron oscillations in our plasmonic cavities, the mode volume is calculated as high as 9.48×10^{-23} approximately $10^{-3}(\lambda_0/n)^3$, where λ_0 is the free-space wavelength, n is the refractive index of the cavity medium (Supplementary Fig.S3). It represents an over 100-folds decrement than the minimum value in PCs, which is set by the diffraction limit as $0.1(\lambda_0/n)^3$ at room temperature[20, 32]. However, this strong confinement needs to pay the cost of strong damping. The quality factors in metals are usually the order of ten[33]. Our dielectric nanostripe arrays can produce a sharp lattice plasmon mode with an improved quality factor $Q = \frac{\lambda}{\Delta\lambda} > 20$ that can be up to ~50 after coating with h-BN/WS_2 heterostructure. Hence, the Purcell factor of our device can reach around 9725 with low losses, which would be very helpful to improve the performance of the modified spontaneous emitters.

To determine the coupling behavior of monolayer WS_2 on the plasmonic nanostripes, we first characterized spontaneous emissions located at the regions with and without h-BN film in Figure 2d. The PL peak intensity at the region stacked few layers h-BN film (blue line) is 4 times stronger than that of the region with only WS_2 (red line) and 15 times stronger than the intrinsic WS_2 monolayer without nanocavities (green line). Compared to h-BN/WS_2 on Si/SiO_2 substrate, where the top h-BN only leads the PL intensity slightly increases (Supplementary Fig.S4), the dielectric nanocavity enhances the light emission apparently, and meanwhile shifts the neutral exciton X_A to low

energy by about 0.01 eV due to the competing combination of band gap normalization and Coulomb screening. Scattering spectra are exhibited in Figure 2e. The phonon scattering mechanism introduced by top h-BN could suppress the exciton diffusion and enhance the exciton formation[27], contributing to neutral exciton X_A at 618 nm. Meanwhile, the trion exciton X_A^- at 640 nm is suppressed due to the reduced exciton mean free path. Besides protecting 2D WS_2 and enhancing its emission, h-BN is purposely introduced because the refractive index of a few layers h-BN ($n \cong 1.85$ for ~10 nm thick layers[34]) is close to that of Al_2O_3 ($n \cong 1.77$) at 618 nm. Hence, the TiO_2 nanostripes are able to be effectively embedded in a uniform index environment, which is critical for sustaining high-quality lattice plasmons[24]. A broad tip appears near 685 nm in both regions, which is caused by inevitable fabrication errors for dielectric nanocavities during the EBL process. The PL spectrum and peak intensity of h-BN/WS_2 heterostructure as a function of excitation power are shown in Figure 2f. As the excitation power increases, the intensity of X_A peak increases and presents an exponential curve dependence in log-log scale with a steady state for peak position and full width at half maximum (FWHM), as shown in Supplementary Fig.S5.

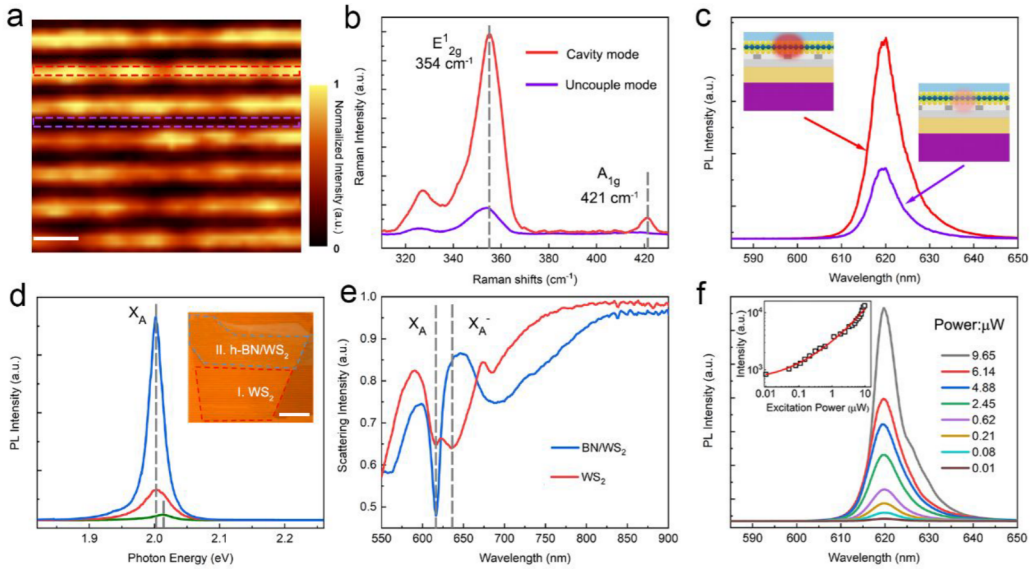

Figure 2. Characteristics of the modified spontaneous emission in our device. (a) PL intensity mapping (integrated into the spectral range from 613.5 to 622 nm) excited by 532 nm laser with the power of 100 nW, and the excitation is polarized along the longitudinal direction. Positions of cavity mode and uncoupled mode are marked by red and purple dash blocks, respectively. The scale bar is 0.5 μm. (b)-(c) Raman (b) and PL (c) spectra of the cavity mode and the uncoupled mode. The side view of h-BN/WS_2 heterostructure on TiO_2 nanocavities is represented in (c) with the two different emission modes. (d) Comparison of emission spectra from different regions. Green line presents the intrinsic monolayer WS_2 on Si/SiO_2 substrate. Inset: optical image of I. WS_2 and II. h-BN/WS_2 regions on nanocavities. The scale bar is 10 μm**.** (e) Scattering spectra of h-BN/WS_2 (blue line) and WS_2 (red line) on the cavity. (f) PL spectra of h-BN/WS_2 on the cavity as a function of excitation power. Inset: peak intensity with increasing excitation power in log-log scale. The red solid line is Lorentzian fits.

Exciton-plasmon coupling dynamics introduced by polarization. To investigate the dynamics of interaction between exciton and plasmon, we performed

polarization-dependent experiments in which the polarization of the excitation light was rotated with respect to the nanostripes. The monolayer WS_2 possesses excitons highly confined in the in-plane direction, thus the orientation of exciton $\vec{\mu}$ can be controlled by the incident linear polarization[35], so the coupling strength of exciton-plasmon is in proportion to $\vec{\mu} \cdot \vec{\varepsilon}$, where ε is the local electric field[20]. Figure 3a shows a polarization series of SE intensity mapping measured at the same nanocavity region. When the excitation is polarized along the longitudinal direction at polarization angle $\theta = 90°$, the coupling strength are the strongest where the orientation of excitation is parallel to longitudinal plasmon mode of nanostripes. As the excitation polarization is rotated towards the transverse direction, the PL intensity becomes weaker gradually with the reduced coupling strength. The corresponding PL spectra are shown in Figure 3b, indicating the main contribution of emission derived from the coupled exciton in plasmonic nanocavities. Similar results for scattering spectra can be seen in Supplementary Fig.S6. The significant change in polarization dependence can be observed in Figure 3c, and the measured polarization ratio of our device is about 40.7% at $\theta = 90°$, which is distinct from the unpolarized PL spectrum in intrinsic monolayer WS_2[36]. In order to demonstrate the scattering behavior of our device at far field, each of the dielectric plasmon scattering was homogeneously recorded by a dark-field microscope under the illumination of white light. The images are displayed by subtracting the background signal, as shown in Figure 3d. However, only the scattering of light from localized variations at the region of h-BN/WS_2 on the nanocavity can contribute to the image with bright and stable red luminescence, the region of

monolayer WS_2 on the nanocavity is invisible and submerged in the background due to lack of h-BN layer. It is clear from Figure 3d that the brightness of emission area can be controlled by the polarization of incident white lights, which reveals that the linear polarization state of incident beam can actively control the exciton-plasmon coupling, leading to total emissions with different intensities. Importantly, such polarization-dependence is an unequivocal proof for the resonant energy transfer theory by dipole-dipole coupling between WS_2 excitons and plasmons.

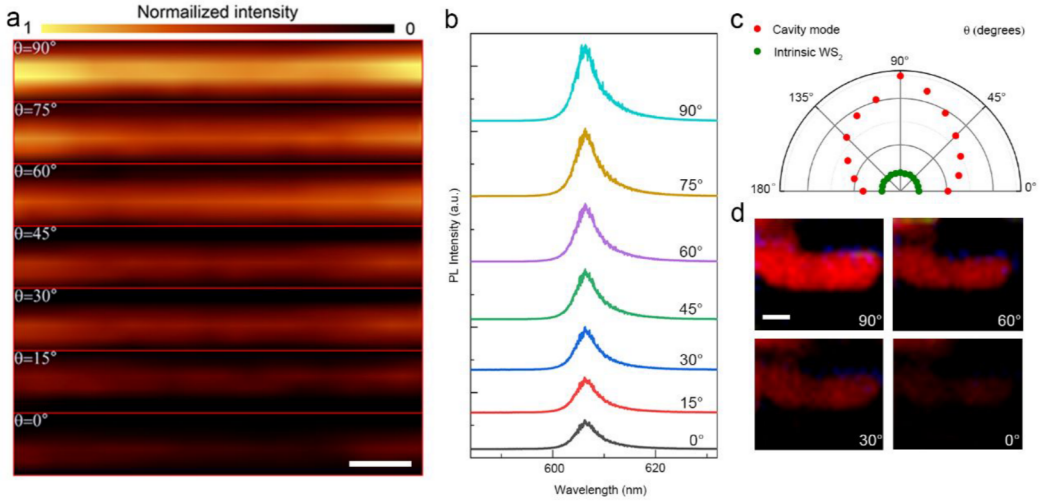

Figure 3. Influence of rotary angle to an incident linear polarization on the exciton-plasmon coupling. (a) Intensity mappings of SE in single nanocavity at $\theta = 90°$ to 0°, where θ presents the angle between polarization direction of incident light and long axis of the nanostripes. The scale bar is 0.5 μm. (b) PL spectra of the device, corresponding to the same polarization configurations in (a). (c) The polar plot represents the emission peak intensity of WS_2 on cavity mode and intrinsic WS_2. (d) Far-field scattering images of the device at $\theta = 0°$, 30°, 60°, 90°, the optical image of WS_2 and h-BN/WS_2 regions is inset of Figure 2d. The scale bar is 10 μm.

Resonant energy transfer mechanism between WS_2 excitons and

plasmons. To gain insight into the energy conversion mechanism of the h-BN/WS_2 emitter, we developed a schematic of band structure model to understand the process of resonant energy transfer in Figure 4a. Under the illumination of polarized light, numbers of bonded excitons are excited and polarized along the same polarization of the incident light. Considering the resonant frequency of TiO_2 nanostripes matching the band gap in monolayer WS_2, the simulated near-field intensity ($|E|^2$) could reveal the generation of cavity mode under polarized excitations, as shown in Figure 4b-e. Significantly, the spatial distribution of $|E|^2$ further supports the polarization characteristic of lattice plasmons, which is produced by the excitation of plasmon resonances next to the surface of the low-index dielectric nanostripes with few-nanometer length. It results in a high LDOS in the near field of the nanocavity to produce strong emission modification.

When these two emitters locate in close proximity to each other, the non-radiative energy exchange will occur efficiently through dipole-dipole coupling, and resonant plasmons in the nanocavity can be seen as the second emitter in this analogy[20]. Once those plasmons in the cavity are excited through the energy transfer at rate Γ_g, they can radiate into free space at rate Γ_r or they can be absorbed and non-radiatively heating at rate Γ_{nr}. The ratio of radiative and non-radiative rates depends on the size and composition of the nanocavity, and the radiation dominating mainly comes from large structures[37, 38], like our low-index dielectric nanostripes. When the plasmons decay occurs faster than excitation of the plasmons, the far field emission rate Γ_{far} can be defined as, $\Gamma_{far} = \Gamma_0 + \Gamma_g\Gamma_r / (\Gamma_r + \Gamma_{nr})$, where the Γ_0 represents the rate of WS_2

radiates directly into free space without the coupling to the nanocavity[20]. The total decay rate of our device also includes the quenching process at rate Γ_q and the non-radiative relaxation process in WS_2 at rate Γ'_{nr}, defined as $\Gamma_{tot} = \Gamma_0 + \Gamma_g + \Gamma_q + \Gamma'_{nr}$. Hence, the emission quantum yield (QY) with the nanocavity approximately is,

$$QY = \frac{\Gamma_{far}}{\Gamma_{tot}} = \frac{\Gamma_0}{\Gamma_{tot}} + \frac{\Gamma_g}{\Gamma_{tot}} \times \frac{\Gamma_r}{\Gamma_r + \Gamma_{nr}} \quad (2)$$

It is thus apparent that the QY can be increased if the Γ_g factor is high. For our devices, a high Γ_g factor mainly relies on the high index contrast between the dielectric emitter (TiO_2: n≅2.60 at 618 nm) and the dielectric environment (Al_2O_3: n≅1.77 at 618 nm)[38].

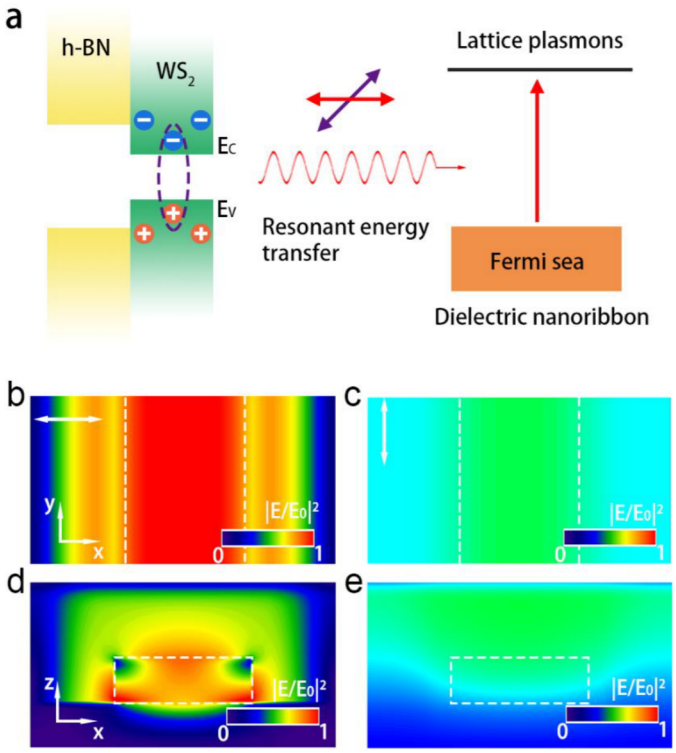

Figure 4. Energy transfer process in exciton-plasmon coupling. (a) Scheme of the resonant energy transfer from WS_2 excitons to lattice plasmons. The orientation of WS_2 exciton (purple arrow) couples with the longitudinal plasmon mode of nanostripes (red arrow), and the modified emission

is produced by the decay of lattice plasmons. (b)-(c) Top view of the simulated near-field distributions by using FDTD at $\theta = 90°$ (b) and 0° (c). The position of nanostripe is highlighted by the white dash line. (d)-(e) Cross-section of the near-field distributions corresponding to (b) and (c), respectively.

Conclusion. In conclusion, we have first demonstrated that integration of h-BN/WS_2 emitter with plasmonic dielectric nanostripes could modify spontaneous emission at room temperature. In general, the low-index dielectric plasmonic nanostructures with less non-radiative losses could form a near-field enhancement surrounding TiO_2 nanostripes, which matches the band gap of monolayer WS_2. Excluding splitting effect caused by strong coupling in noble metal structure, the resonant energy transfer in dielectric plasmonic nanostructures leads to a remarkable enhancement for Purcell factor over 9700. We use few layers h-BN as the top layer to improve the cavity quality and protect emitters, which provides a novel design for 2D heterostructure emitters. To support the resonant energy transfer mechanism and shed further light on it, we perform a series of polarization experiments to demonstrate this dipole-dipole coupling between excitons of WS_2 and plasmons of nanocavities in the energy transfer process, which agrees well with our simulated results. Importantly, our results reveal a path to investigate the exciton-plasmon dynamics and deterministically achieve the Purcell enhancement for the spontaneous emitter by using dielectric plasmonic nanocavities. In particular, it has potential applications in quantum information processing and integrated 2D on-chip devices.

Methods. *Device Fabrication.* Si/SiO_2 substrates were first coated with 100 nm thick Au layers and 10 nm thick Al_2O_3 using electron-beam evaporation. Then, we fabricated nanocavities on it by electron-beam lithography (resist: PMMA 950 A2). And 45 nm TiO_2 layers was deposited on the substrate using electron beam evaporation. The monolayer WS_2 and few layers h-BN were prepared by mechanical exfoliation and transferred onto the nanocavity by polydimethylsiloxane (PDMS).

FDTD simulations. The finite-different time-domain (FDTD) solutions was used to simulate the local field enhancement of the fabricated nanostructures and their scattering cross sections. A unit cell of the nanocavities was simulated under periodic boundary conditions along the *x* and *y* axes, and perfectly matched layers along the propagation of electromagnetic waves (*z* axis), which consisted of a semi-infinite Si layer, 100 nm Au layer, 10 nm Al_2O_3 layer and an TiO_2 nanostripe with the same size as the experiment. Plane wave sources with linearly polarizations were used to excite the TiO_2 nanostripe structure. We used the experimental dielectric function from Johnson and Christy for the Au material. Refractive indexes ofTiO_2 and SiO_2 are n=2.60 and 1.45 respectively. The calculation of mode volume is defined as,

$$V_0 = \frac{\int \varepsilon(\boldsymbol{r})|\boldsymbol{E}(\boldsymbol{r})|^2 d^3\boldsymbol{r}}{max\left(\varepsilon(\boldsymbol{r})|\boldsymbol{E}(\boldsymbol{r})|^2\right)}$$

where $\varepsilon(\boldsymbol{r})$ is the dielectric permittivity and $\boldsymbol{E}(\boldsymbol{r})$ is electric field, $\boldsymbol{r}$ presents the spatial location.

Optical characterization. The PL spectra were measured by using a confocal microscope system (WITec, Alpha 300) under the excitation of a YAG 532 nm laser

with an integration time of 5 s for every PL measurement. The scanning step of PL mapping is about 10 nm under a 100 × objective (Zeiss, NA=0.95, WD = 0.31 mm). The scattering spectra were obtained by a commercial hyperspectral imaging system (HIS V3, CytoViva Co.). A polarizer is inserted to generate linearly polarized white light.

Data availability. The data that support the findings of this study are available from the authors on reasonable request.

Acknowledgements

This work is supported by Start-up funds of Wuhan University, Singapore National Research Foundation (NRF) under the Competitive Research Programs (NRF-CRP-21-2018-0007).

Author Information

Corresponding Authors

*E-mail: z.liu@ntu.edu.sg.

*E-mail: zhyfang@pku.edu.cn.

*E-mail: yu.ting@whu.edu.cn.

Notes

The authors declare no competing financial interest.

References

(1) Cong, C.; Shang, J.; Wang, Y.; Yu, T. Optical Properties of 2D Semiconductor WS_2. *Adv. Opt. Mater.* **2018,** 6, (1), 1700767.

(2) Tan, C.; Lai, Z.; Zhang, H. Ultrathin Two-Dimensional Multinary Layered Metal Chalcogenide

Nanomaterials. *Adv. Mater.* **2017,** 29, (37), 1701392.

(3) Wang, Q. H.; Kalantar-Zadeh, K.; Kis, A.; Coleman, J. N.; Strano, M. S. Electronics and optoelectronics of two-dimensional transition metal dichalcogenides. *Nat. Nanotechnol.* **2012,** 7, (11), 699-712.

(4) Zhou, J.; Lin, J.; Huang, X.; Zhou, Y.; Chen, Y.; Xia, J.; Wang, H.; Xie, Y.; Yu, H.; Lei, J.; Wu, D.; Liu, F.; Fu, Q.; Zeng, Q.; Hsu, C. H.; Yang, C.; Lu, L.; Yu, T.; Shen, Z.; Lin, H.; Yakobson, B. I.; Liu, Q.; Suenaga, K.; Liu, G.; Liu, Z. A library of atomically thin metal chalcogenides. *Nature* **2018,** 556, (7701), 355-359.

(5) Wu, L.; Cong, C.; Yang, W.; Chen, Y.; Shao, Y.; Do, T. T. H.; Wen, W.; Feng, S.; Zou, C.; Zhang, H.; Du, B.; Cao, B.; Shang, J.; Xiong, Q.; Loh, K. P.; Yu, T. Observation of Strong Valley Magnetic Response in Monolayer Transition Metal Dichalcogenide Alloys of $Mo_{0.5}W_{0.5}Se_2$ and $Mo_{0.5}W_{0.5}Se_2/WS_2$ Heterostructures. *Acs Nano* **2021,** 15, (5), 8397-8406.

(6) Yin, X.; Ye, Z.; Chenet, D. A.; Ye, Y.; O'Brien, K.; Hone, J. C.; Zhang, X. Edge Nonlinear Optics on a MoS_2 Atomic Monolayer. *Science* **2014,** 344, 488-490.

(7) Liu, F.; Zhou, J.; Zhu, C.; Liu, Z. Electric Field Effect in Two-Dimensional Transition Metal Dichalcogenides. *Adv. Funct. Mater.* **2017,** 27, (19), 1602404.

(8) Darlington, T. P.; Carmesin, C.; Florian, M.; Yanev, E.; Ajayi, O.; Ardelean, J.; Rhodes, D. A.; Ghiotto, A.; Krayev, A.; Watanabe, K.; Taniguchi, T.; Kysar, J. W.; Pasupathy, A. N.; Hone, J. C.; Jahnke, F.; Borys, N. J.; Schuck, P. J. Imaging strain-localized excitons in nanoscale bubbles of monolayer WSe_2 at room temperature. *Nat. Nanotechnol.* **2020,** 15, 854–860.

(9) Shang, J.; Cong, C.; Wang, Z.; Peimyoo, N.; Wu, L.; Zou, C.; Chen, Y.; Chin, X. Y.; Wang, J.; Soci, C.; Huang, W.; Yu, T. Room-temperature 2D semiconductor activated vertical-cavity surface-

emitting lasers. *Nat. Commun.* **2017,** 8, (1), 543.

(10) Chen, J. H.; Tan, J.; Wu, G. X.; Zhang, X. J.; Xu, F.; Lu, Y. Q. Tunable and enhanced light emission in hybrid WS2-optical-fiber-nanowire structures. *Light Sci. Appl.* **2019,** 8, 8.

(11) Wu, S.; Buckley, S.; Schaibley, J. R.; Feng, L.; Yan, J.; Mandrus, D. G.; Hatami, F.; Yao, W.; Vuckovic, J.; Majumdar, A.; Xu, X. Monolayer semiconductor nanocavity lasers with ultralow thresholds. *Nature* **2015,** 520, (7545), 69-72.

(12) Luo, Y.; Shepard, G. D.; Ardelean, J. V.; Rhodes, D. A.; Kim, B.; Barmak, K.; Hone, J. C.; Strauf, S. Deterministic coupling of site-controlled quantum emitters in monolayer WSe_2 to plasmonic nanocavities. *Nat. Nanotechnol.* **2018,** 13, (12), 1137-1142.

(13) Wang, Q.; Guo, J.; Ding, Z.; Qi, D.; Jiang, J.; Wang, Z.; Chen, W.; Xiang, Y.; Zhang, W.; Wee, A. T. S. Fabry-Perot Cavity-Enhanced Optical Absorption in Ultrasensitive Tunable Photodiodes Based on Hybrid 2D Materials. *Nano Lett.* **2017,** 17, (12), 7593-7598.

(14) Reed, J. C.; Zhu, A. Y.; Zhu, H.; Yi, F.; Cubukcu, E. Wavelength tunable microdisk cavity light source with a chemically enhanced MoS_2 emitter. *Nano Lett.* **2015,** 15, (3), 1967-1971.

(15) Flatten, L. C.; He, Z.; Coles, D. M.; Trichet, A. A. P.; Powell, A. W.; Taylor, R. A.; Warner, J. H.; Smith, J. M. Room-temperature exciton-polaritons with two-dimensional WS_2. *Sci. Rep.* **2016,** 6, (1), 33134.

(16) Peyskens, F.; Chakraborty, C.; Muneeb, M.; Van Thourhout, D.; Englund, D. Integration of single photon emitters in 2D layered materials with a silicon nitride photonic chip. *Nat. Commun.* **2019,** 10, (1), 4435.

(17) Du, B.; Lin, L.; Liu, W.; Zu, S.; Yu, Y.; Li, Z.; Kang, Y.; Peng, H.; Zhu, X.; Fang, Z. Plasmonic hot electron tunneling photodetection in vertical Au-graphene hybrid nanostructures. *Laser Photonics*

Rev. **2017,** 11, (1), 1600148.

(18) Cuartero-Gonzalez, A.; Sanders, S.; Zundel, L.; Fernandez-Dominguez, A. I.; Manjavacas, A. Super- and Subradiant Lattice Resonances in Bipartite Nanoparticle Arrays. *Acs Nano* **2020,** 14, (9), 11876-11887.

(19) Brongersma, M. L.; Halas, N. J.; Nordlander, P. Plasmon-induced hot carrier science and technology. *Nat. Nanotechnol.* **2015,** 10, (1), 25-34.

(20) Pelton, M. Modified spontaneous emission in nanophotonic structures. *Nat. Photonics* **2015,** 9, (7), 427-435.

(21) Khurgin, J. B. How to deal with the loss in plasmonics and metamaterials. *Nat. Nanotechnol.* **2015,** 10, (1), 2-6.

(22) Clavero, C. Plasmon-induced hot-electron generation at nanoparticle/metal-oxide interfaces for photovoltaic and photocatalytic devices. *Nat. Photonics* **2014,** 8, (2), 95-103.

(23) Xie, Y. Y.; Ni, P. N.; Wang, Q. H.; Kan, Q.; Briere, G.; Chen, P. P.; Zhao, Z. Z.; Delga, A.; Ren, H. R.; Chen, H. D.; Xu, C.; Genevet, P. Metasurface-integrated vertical cavity surface-emitting lasers for programmable directional lasing emissions. *Nat. Nanotechnol.* **2020,** 15, (2), 125-130.

(24) Fernandez-Bravo, A.; Wang, D.; Barnard, E. S.; Teitelboim, A.; Tajon, C.; Guan, J.; Schatz, G. C.; Cohen, B. E.; Chan, E. M.; Schuck, P. J.; Odom, T. W. Ultralow-threshold, continuous-wave upconverting lasing from subwavelength plasmons. *Nat. Mater.* **2019,** 18, (11), 1172-1176.

(25) Ye, Z.; Cao, T.; O'Brien, K.; Zhu, H.; Yin, X.; Wang, Y.; Louie, S. G.; Zhang, X. Probing excitonic dark states in single-layer tungsten disulphide. *Nature* **2014,** 513, (7517), 214-218.

(26) Zhao, L.; Shang, Q.; Li, M.; Liang, Y.; Li, C.; Zhang, Q. Strong exciton-photon interaction and lasing of two-dimensional transition metal dichalcogenide semiconductors. *Nano Res.* **2021,** 14, 1937–

1954.

(27) Fu, Y.; He, D.; He, J.; Bian, A.; Zhang, L.; Liu, S.; Wang, Y.; Zhao, H. Effect of Dielectric Environment on Excitonic Dynamics in Monolayer WS_2. *Advanced Materials Interfaces* **2019,** 6, (23), 1901307.

(28) Li, B.; Zu, S.; Zhou, J.; Jiang, Q.; Du, B.; Shan, H.; Luo, Y.; Liu, Z.; Zhu, X.; Fang, Z. Single-Nanoparticle Plasmonic Electro-optic Modulator Based on MoS_2 Monolayers. *Acs Nano* **2017,** 11, (10), 9720-9727.

(29) Dong, J.; Chen, S.; Huang, G.; Wu, Q.; Huang, X.; Wang, L.; Zhang, Y.; Ao, X.; He, S. Low-Index-Contrast Dielectric Lattices on Metal for Refractometric Sensing. *Adv. Opt. Mater.* **2020,** 8, (21), 2000877.

(30) Du, B.; Yang, W.; Jiang, Q.; Shan, H.; Luo, D.; Li, B.; Tang, W.; Lin, F.; Shen, B.; Gong, Q.; Zhu, X.; Zhu, R.; Fang, Z. Plasmonic-Functionalized Broadband Perovskite Photodetector. *Adv. Opt. Mater.* **2018,** 6, (8), 1701271.

(31) Liu, N.; Gocalinska, A.; Justice, J.; Gity, F.; Povey, I.; McCarthy, B.; Pemble, M.; Pelucchi, E.; Wei, H.; Silien, C.; Xu, H.; Corbett, B. Lithographically Defined, Room Temperature Low Threshold Subwavelength Red-Emitting Hybrid Plasmonic Lasers. *Nano Lett.* **2016,** 16, (12), 7822-7828.

(32) Pelton, M.; Storm, S. D.; Leng, H. Strong coupling of emitters to single plasmonic nanoparticles: exciton-induced transparency and Rabi splitting. *Nanoscale* **2019,** 11, (31), 14540-14552.

(33) Russell, K. J.; Liu, T.-L.; Cui, S.; Hu, E. L. Large spontaneous emission enhancement in plasmonic nanocavities. *Nat. Photonics* **2012,** 6, (7), 459-462.

(34) Fali, A.; White, S. T.; Folland, T. G.; He, M.; Aghamiri, N. A.; Liu, S.; Edgar, J. H.; Caldwell, J. D.; Haglund, R. F.; Abate, Y. Refractive Index-Based Control of Hyperbolic Phonon-Polariton

Propagation. *Nano Lett.* **2019,** 19, (11), 7725-7734.

(35) Santhosh, K.; Bitton, O.; Chuntonov, L.; Haran, G. Vacuum Rabi splitting in a plasmonic cavity at the single quantum emitter limit. *Nat. Commun.* **2016,** 7, ncomms11823.

(36) Dasgupta, A.; Yang, X.; Gao, J. Nonlinear Beam Shaping with Binary Phase Modulation on Patterned WS2 Monolayer. *ACS Photonics* **2020,** 7, (9), 2506-2514.

(37) Kim, J. H.; Lee, H. S.; An, G. H.; Lee, J.; Oh, H. M.; Choi, J.; Lee, Y. H. Dielectric Nanowire Hybrids for Plasmon-Enhanced Light-Matter Interaction in 2D Semiconductors. *Acs Nano* **2020,** 14, (9), 11985-11994.

(38) Yang, Y.; Miller, O. D.; Christensen, T.; Joannopoulos, J. D.; Soljacic, M. Low-Loss Plasmonic Dielectric Nanoresonators. *Nano Lett.* **2017,** 17, (5), 3238-3245.

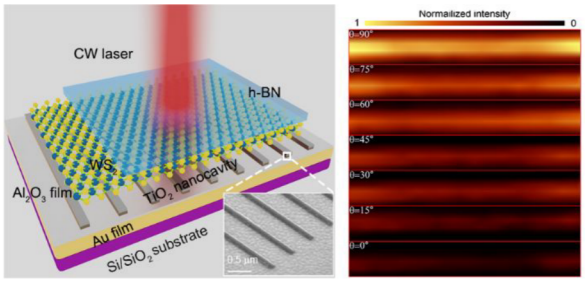

TOC Graphic